

**Giant crystal-electric-field effect and complex magnetic behavior
in single-crystalline CeRh₃Si₂**

A. P. Pikul, D. Kaczorowski, Z. Gajek, J. Stępień–Damm

*Institute of Low Temperature and Structure Research,
Polish Academy of Sciences, P Nr 1410, 50–950 Wrocław, Poland*

A. Ślebarski

Institute of Physics, University of Silesia, 40–007 Katowice, Poland

M. Werwiński, A. Szajek

Institute of Molecular Physics, Polish Academy of Sciences, 60–179 Poznań, Poland

(Dated: October 17, 2018)

Abstract

Single-crystalline CeRh_3Si_2 was investigated by means of x-ray diffraction, magnetic susceptibility, magnetization, electrical resistivity, and specific heat measurements carried out in wide temperature and magnetic field ranges. Moreover, the electronic structure of the compound was studied at room temperature by cerium core-level x-ray photoemission spectroscopy (XPS). The physical properties were analyzed in terms of crystalline electric field and compared with results of ab-initio band structure calculations performed within the density functional theory approach. The compound was found to crystallize in the orthorhombic unit cell of the ErRh_3Si_2 type (space group $\text{Imma} - \text{No.74}$, Pearson symbol: oI24) with the lattice parameters: $a = 7.1330(14) \text{ \AA}$, $b = 9.7340(19) \text{ \AA}$, and $c = 5.6040(11) \text{ \AA}$. Analysis of the magnetic and XPS data revealed the presence of well localized magnetic moments of trivalent cerium ions. All physical properties were found to be highly anisotropic over the whole temperature range studied, and influenced by exceptionally strong crystalline electric field with the overall splitting of the $4f^1$ ground multiplet exceeding 5700 K. Antiferromagnetic order of the cerium magnetic moments at $T_N = 4.70(1) \text{ K}$ and their subsequent spin rearrangement at $T_t = 4.48(1) \text{ K}$ manifest themselves as distinct anomalies in the temperature characteristics of all investigated physical properties and exhibit complex evolution in an external magnetic field. A tentative magnetic $B-T$ phase diagram, constructed for B parallel to the b -axis being the easy magnetization direction, shows very complex magnetic behavior of CeRh_3Si_2 , similar to that recently reported for an isostructural compound CeIr_3Si_2 . The electronic band structure calculations corroborated the antiferromagnetic ordering of the cerium magnetic moments and well reproduced the experimental XPS valence band spectrum.

PACS numbers: 75.10.Dg (crystal-field theory and spin Hamiltonians), 75.30.Gw (magnetic anisotropy), 75.30.Kz (magnetic transitions), 75.50.Ee (antiferromagnetics), 71.20.Lp (electronic structure of bulk materials)

I. INTRODUCTION

The phase diagram Ce-Rh-Si comprises twenty five ternary phases with well defined crystal structures [1]. However, physical properties have been reported for only a few of them, namely: CeRhSi₂ and Ce₂Rh₃Si₅ (both described in the literature as intermediate valence systems [2–4]), Ce₃Rh₃Si₂ (exhibiting complex long-range magnetic ordering [5]), CeRh₂Si₂ and CeRhSi₃ (antiferromagnetic heavy-fermion systems [6,7]). The two latter phases are known as pressure-induced superconductors [8–11]. While in CeRh₂Si₂ the superconductivity seems to replace the antiferromagnetism [8,9], in CeRhSi₃ it develops deeply inside the ordered state [10,11]. Most interesting, the superconductivity in non-centrosymmetric CeRhSi₃ involves spin-fluctuations-assisted triplet pairing [11]. In the context of recent findings for the Ce–Rh–Si ternaries, comprehensive physical characterization of other (hitherto unknown or hardly studied) phases from the system seems quite desirable. To the best of our knowledge existence of CeRh₃Si₂ has for the first time been reported by Morozkin et al. [12], yet without any crystallographic or physical data. Then, CeRh₃Si₂ has been found as an impurity phase in polycrystalline CeRh₂Si₂ [13]. In the latter study it has been established that the compound crystallizes with an orthorhombic crystal structure and exhibits an antiferromagnetic phase transition at $T_N = 5$ K [13].

Here we report the results of our investigation of the crystal structure and the basic physical properties of CeRh₃Si₂ performed on single-crystalline specimens in wide temperature and magnetic field ranges. The experimental characterization is accompanied by the results of ab-initio calculations of the electronic band structure. Short accounts on the work presented in this paper were given in conference communications [14,15].

II. EXPERIMENTAL AND COMPUTATIONAL DETAILS

A single crystal of CeRh₃Si₂ was grown by the Czochralski pulling method employing a tetra-arc furnace under protective ultra-pure (4.8N, BOC Gases) argon atmosphere, which was additionally titanium-gettered during the whole growing process. The starting polycrystalline melt was prepared from pieces of Ce (3N, Ames Laboratory), Rh ingot (3N, Chempur) and Si chips (6N, Chempur). The pulling rate was 10 mm/h, and the copper heart rotation speed was 3 rpm. The final ingot of CeRh₃Si₂ was about 4 mm in diameter

and 40 mm in length. From this single-crystalline rod a fragment of about 20 mm in length was cut for experimental studies. The crystal was wrapped in Ta-foil, sealed in an evacuated silica tube, and annealed at 900°C for 2 weeks. The quality of the product was verified by means of x-ray powder diffraction measurements performed on a pulverized piece of the crystal (Stoe diffractometer with Cu $K\alpha$ radiation) and microprobe analysis (Phillips 515 scanning electron microscope equipped with an EDAX PV 9800 spectrometer). The entire X-ray diffractogram was indexed with an orthorhombic unit cell, and the sample was found to be single phase. Additionally, a polycrystalline sample of an isostructural LaRh_3Si_2 compound, being a non-magnetic counterpart of CeRh_3Si_2 , was prepared by conventional arc melting stoichiometric amounts of the constituents. X-ray powder diffraction experiments proved that the La-based phase is indeed isostructural to CeRh_3Si_2 .

The crystal structure of CeRh_3Si_2 was also examined on a small single-crystalline fragment using a four-circle diffractometer equipped with a CCD camera (Kuma Diffraction KM-4 with graphite-monochromatized Mo $K\alpha$ radiation). Crystal structure refinement was performed using full-matrix least-squares on F^2 as a refinement method and applying the SHELXL-97 program [16]. The magnetic properties were studied at temperatures ranging from 1.7 K up to 300 K in applied magnetic fields up to 5 T using a Quantum Design MPMS-5 superconducting quantum interference device (SQUID) magnetometer. The electrical resistivity was measured in the temperature range 1.5 – 300 K employing standard DC four-point technique. Electrical contacts to bar-shaped specimens were made by spot welding. The heat capacity was measured in the temperature interval 350 mK – 300 K in applied magnetic fields up to 9 T using a Quantum Design PPMS platform. For these experiments the thermal relaxation method [17] was applied with 2% heat pulses and Apiezon N vacuum grease as a sample mounting medium. The x-ray photoelectron spectroscopy (XPS) measurements were carried out at room temperature with monochromatized Al $K\alpha$ radiation using a PHI-5700 ESCA spectrometer. The sample of CeRh_3Si_2 was scraped with a diamond file under high vacuum immediately before recording a spectrum.

The electronic structure calculations were performed with a density functional theory (DFT) [18] using the full-potential linearized augmented plane wave (FP LAPW) method implemented in the latest version (Wien2k) of the original WIEN code [19]. In the Wien2k code calculations the scalar relativistic approach was implemented with the spin-orbit interactions taken into account by using the second variational method [20]. The exchange

correlation potential in the local (spin) density approximation (LSDA) was assumed in the form proposed by Perdew, Burke, and Ernzerhof [21] using the generalized gradient approximation. Furthermore, to improve the description of the strongly correlated 5f electrons, the on-site Coulomb energy U correction and exchange J parameters were introduced within the LSDA+U approach [22,23]. In our case we used $U_{\text{eff}} = U - J$, setting $J = 0$. Another approach applied by us to reduce the discrepancy between the DFT magnetic moments and experimental ones was taking into account the so-called orbital polarization (OP) term, as proposed by Brooks [24] and Eriksson et al. [25,26]. The number of k -points was 2000 in the Brillouin zone (BZ), which corresponds to 240 points in an irreducible wedge of the BZ for all methods of calculations applied in this paper. For the BZ integration, a tetrahedron method was used [27]. The self-consistency criterion was equal 10^{-6} Ry for the total energy. The calculations were performed for lattice constants and atomic positions in the unit cell described below in Sec. III A. The theoretical x-ray photoemission spectra were obtained from the calculated densities of electronic states (DOS) convoluted by a Gaussian with a half-width δ equal to 0.3 eV and scaled using the proper photoelectronic cross sections for partial states [28].

III. RESULTS AND DISCUSSION

A. Crystal structure

The crystal structure refinement (see Tab. I) performed for single-crystalline CeRh_3Si_2 confirmed that the compound crystallizes in the orthorhombic symmetry with the space group Imma (No.74, Pearson symbol $\text{oI}24$) and that it is isostructural with ErRh_3Si_2 [29]. Refined lattice parameters are: $a = 7.1330(14)$ Å, $b = 9.7340(19)$ Å, $c = 5.6040(11)$ Å, and the atomic coordinates are listed in Tab. II. Figure 1 presents the structure of CeRh_3Si_2 viewed along the a -axis.

The ErRh_3Si_2 -type crystal structure was described in detail in Ref. 29. It represents a deformed superstructure of the hexagonal CaCu_5 -type structure with $a = 2c_h$, $b = \sqrt{3}a_h$, and $c = a_h$, where a_h and c_h are the lattice parameters of the parent hexagonal unit cell. The characteristic features of this atom arrangement are a honeycomb-like network of the Rh and Si atoms within the bc plane and zigzag chains of the Ce atoms along the a -axis (see

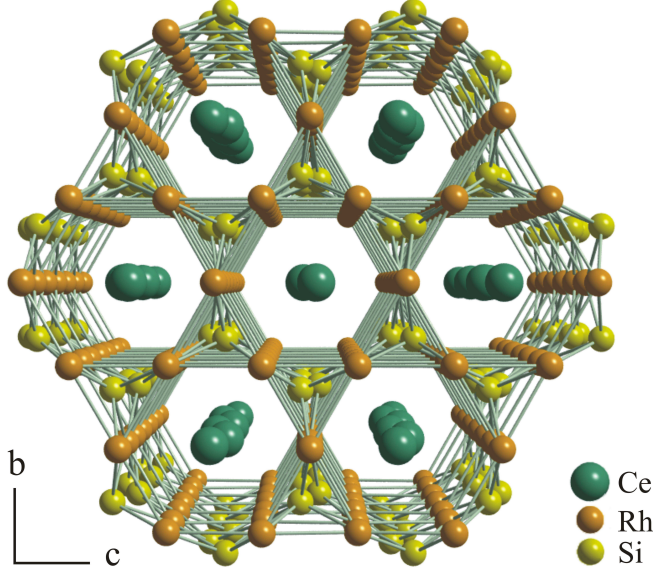


FIG. 1: (Color online) Crystal structure of CeRh_3Si_2 .

Fig. 1).

B. Magnetic properties

Figures 2(a,b) present the magnetic susceptibility χ of CeRh_3Si_2 measured as a function of temperature T in a magnetic field B of 0.5 T applied parallel to the main crystallographic directions. Sharp susceptibility maxima at about 4.5 K, best visible on the $\chi_b(T)$ curve measured along the b -axis [see Fig. 2(a)], manifest the onset of an antiferromagnetically ordered state. Below 4.5 K the susceptibility χ_b does not decrease significantly, as expected for simple antiferromagnets, but saturates at low temperatures, hence suggesting more complex magnetic behavior. The anomaly at 4.5 K is only slightly weaker for the c -axis, and the behavior of χ_c in the ordered region is similar to that of χ_b . On the contrary, the a -axis susceptibility is featureless and very small, thus indicating that the magnetic moments are confined to the bc plane of the unit cell. A distinct difference of $\chi_a(T)$ as compared to the other two components is observed also in the paramagnetic state [see Fig. 2(b)]. At room temperature, the ratio χ_b/χ_a is about 4, and it increases with decreasing temperature down to 200 K, where it is larger than 6. The $\chi_a^{-1}(T)$ variation exhibits strongly curvilinear shape in the whole T -range studied. In contrast, the $\chi_b^{-1}(T)$ and $\chi_c^{-1}(T)$ curves are almost identical and exhibit nearly linear behavior characteristic of systems with well localized magnetic

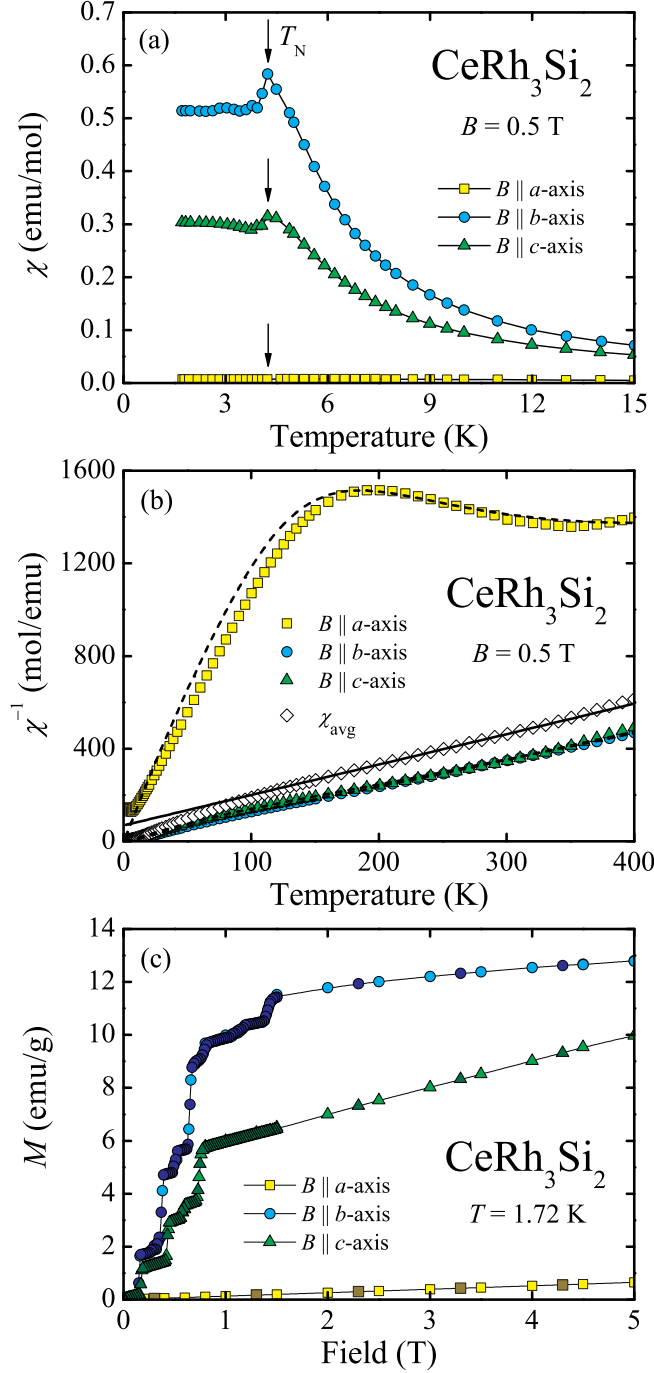


FIG. 2: (Color online) (a) Low-temperature magnetic susceptibility of single-crystalline CeRh_3Si_2 measured in external magnetic field B applied parallel to the principal crystallographic axes. The arrows mark the Néel temperature; the solid lines serve as a guide for the eye. (b) Temperature variations of the inverse magnetic susceptibility of the compound; χ_{avg}^{-1} represents the inverse average magnetic susceptibility. The solid line is a fit of the Curie–Weiss law to the experimental data; the dashed curves represent the fits described in Sec. III E. (c) Magnetization as a function of applied magnetic field measured for single-crystalline CeRh_3Si_2 in zero-field (bright symbols) and field cooling (dark symbols) regimes, along the principal crystallographic axes. The solid lines serve as guides for the eye.

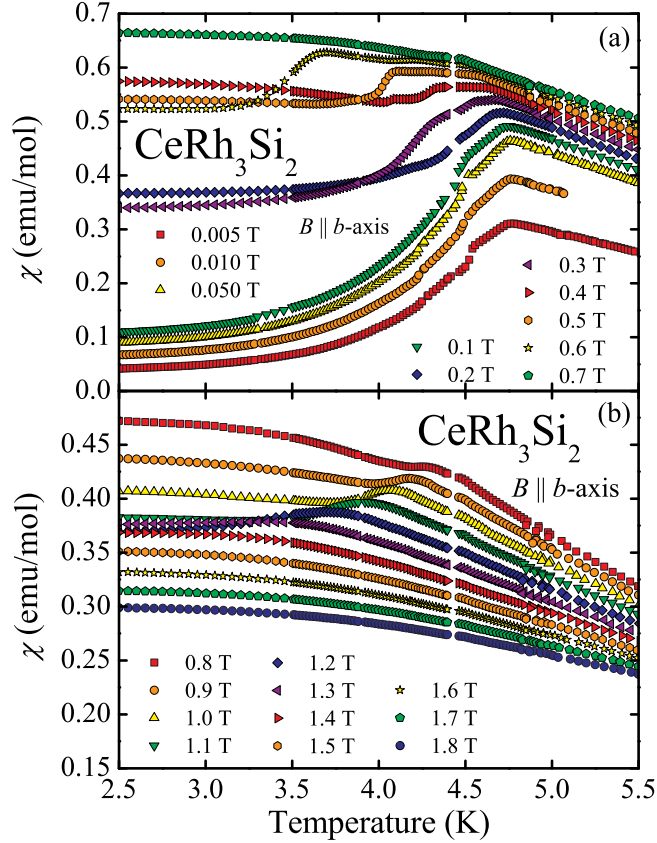


FIG. 3: (Color online) Temperature dependencies of the magnetic susceptibility of single-crystalline CeRh_3Si_2 measured in different applied magnetic fields B parallel to the b -axis. For the sake of clarity the curves are shifted up.

moments. The overall behavior of the magnetic susceptibility of CeRh_3Si_2 implies huge magnetocrystalline anisotropy due to strong crystal field interactions (cf. Sec. III E).

As can be seen in Fig. 2(b), the inverse average "polycrystalline" magnetic susceptibility χ_{avg}^{-1} [defined as $\chi_{\text{avg}} = \frac{1}{3}(\chi_a + \chi_b + \chi_c)$] follows above about 150 K the Curie-Weiss law with the effective magnetic moment $\mu_{\text{eff}} = 2.47 \mu_B$ and the paramagnetic Curie temperature $\theta_{\text{CW}} = -52 \text{ K}$ [see the straight solid line in Fig. 2(b)]. The experimental value of μ_{eff} is close to that calculated for a free Ce^{3+} ion ($g\sqrt{j(j+1)} = 2.54$), and thus indicates the presence of well localized magnetic moments. The negative value of θ_{CW} hints at antiferromagnetic character of the magnetic exchange interactions, in line with the AFM ordering observed below 4.5 K.

Figure 2(c) shows the magnetization of CeRh_3Si_2 measured at 1.72 K as a function of the magnetic field strength. Here the complex magnetic behavior of the compound manifests

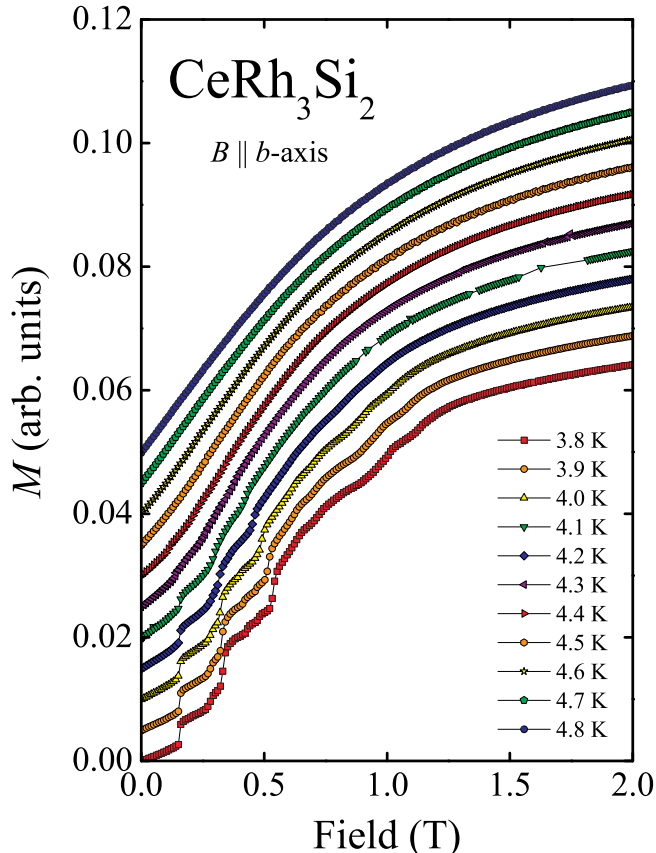


FIG. 4: (Color online) Isothermal magnetization of single-crystalline CeRh_3Si_2 measured with the magnetic field applied along the b -axis at several different temperatures from the ordered region. The curves are shifted up for the sake of clarity.

itself as cascades of metamagnetic-like transitions in $M(B)$ measured along the b - and c -axes. For the former direction of the magnetic field one observes some saturation above about 1.5 T at a value $\mu_s = 12.8$ emu/g corresponding to about $1.16 \mu_B$. In the case of $B \parallel c$ -axis, the magnetization increases linearly with increasing B reaching in 5 T a value of about $0.9 \mu_B$. In turn, for $B \parallel a$ -axis the magnetization is a linear function of the applied field in the entire range studied, and the value of M measured at 5 T is nearly 20 times smaller than that observed for $B \parallel b$ -axis. The overall behavior of $M(B)$ is reminiscent of that reported for CeSb [30,31], TbNi_2Si_2 [32], and TbNi_2Ge_2 [33], which are commonly called "devil's staircase" systems (for short review and discussion see Sec. IV).

In order to shed more light on the nontypical temperature variation of the magnetic susceptibility below 4.5 K [Fig. 2(a)] we performed a series of additional measurements of $\chi_b(T)$, with increased density of the data points. As can be inferred from Fig. 3, in the

TABLE I: Crystallographic and structure refinement data for single-crystalline CeRh₃Si₂.

Empirical formula	Ce _{0.50} Rh _{1.50} Si
Formula weight	252.51 g/mol
Temperature	293(2) K
Wavelength	0.71073 Å
Crystal system, space group	orthorhombic, Imma
Unit cell dimensions	$a = 7.1330(14)$ Å, $\alpha = 90^\circ$ $b = 9.7340(19)$ Å, $\beta = 90^\circ$ $c = 5.6040(11)$ Å, $\gamma = 90^\circ$
Unit cell volume	389.10(13) Å ³
Z	4
Calculated density	8.621 Mg/m ³
Absorption coefficient	24.354 mm ⁻¹
$F(000)$	884
θ range for data collection	4.19° ÷ 45.28°
Limiting indices	$-13 \leq h \leq 9$ $-12 \leq k \leq 19$ $-10 \leq l \leq 10$
Reflections collected / unique	4366 / 840 [$R(\text{int}) = 0.0465$]
Completeness to $\theta = 45.28$	93.8 %
Refinement method	Full-matrix least-squares on F^2
Data / restraints / parameters	840 / 0 / 22
Goodness-of-fit on F^2	1.010
Final R indices [$I > 2\sigma(I)$]	$R_1 = 0.0287$, $wR_2 = 0.0509$
R indices (all data)	$R_1 = 0.0432$, $wR_2 = 0.0524$
Extinction coefficient	0.0356(8)
Largest diff. peak and hole	2.707 eÅ ⁻³ and -3.148 eÅ ⁻³

TABLE II: Atomic coordinates and equivalent isotropic thermal displacement parameters for CeRh_3Si_2 . U_{eq} was defined as one third of the trace of the orthogonalized U_{ij} tensor.

Atom	$x [\times 10^4]$	$y [\times 10^4]$	$z [\times 10^4]$	$U_{\text{eq}} [\times 10^3 \text{\AA}^2]$
Ce	0	7500	2160(1)	8(1)
Rh(1)	2172(1)	5000	0	6(1)
Rh(2)	-2500	7500	-2500	8(1)
Si	0	9215(2)	6996(2)	7(1)

TABLE III: Anisotropic thermal displacement parameters ($\times 10^3 \text{\AA}^2$) for CeRh_3Si_2 . The anisotropic displacement factor exponent takes the form: $-2\pi^2[h^2a^2U_{11} + \dots + 2hkabU_{12}]$.

Atom	U_{11}	U_{22}	U_{33}	U_{23}	U_{13}	U_{12}
Ce	8(1)	7(1)	8(1)	0	0	0
Rh(1)	7(1)	6(1)	5(1)	1(1)	0	0
Rh(2)	13(1)	4(1)	7(1)	0	-2(1)	0
Si	6(1)	9(1)	7(1)	-1(1)	0	0

lowest magnetic field studied (i.e. $B = 0.005$ T) the magnetic order in CeRh_3Si_2 sets in already at $T_{\text{N}} = 4.7$ K. The Néel temperature decreases with increasing field, as expected for antiferromagnets. In a field of 0.5 T, T_{N} is reduced to about 4.5 K, marked by an arrow in Fig. 2(a). Moreover, the high resolution measurements revealed the presence of some spin rearrangement, which takes place just below T_{N} and therefore is hardly visible in Fig. 2(a). In 0.005 T, this spontaneous change of the magnetic structure manifests itself as a tiny anomaly in the $\chi(T)$ curve at $T_{\text{t}} = 4.5$ K, which develops with increasing field into a clear kink moving down on the temperature scale. The latter observation suggests that the antiferromagnetic character of the magnetic order is retained below T_{t} . The plateau visible in 0.5 T below 4 K [Fig. 2(a)] apparently results from superposition of low-temperature slopes of the anomalies at T_{N} and T_{t} , and another, field-induced phase transition. It is well visible in Fig. 3 in the field range $0.7 \text{ T} \leq B \leq 0.9 \text{ T}$ as a broad ferromagnetic-like hump dominating the susceptibility below T_{t} . Unfortunately, complex shape of the $\chi(T)$ curves does not allow us to determine the exact temperature at which the latter contribution sets

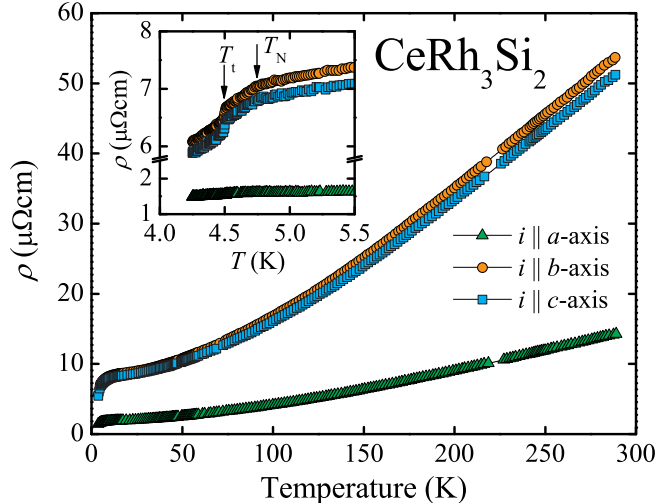


FIG. 5: (Color online) Electrical resistivity of single-crystalline CeRh_3Si_2 measured as a function of temperature with electrical current i flowing along the principal crystallographic directions; solid lines serve as a guide for the eye. The inset: low temperature region; the arrows mark magnetic transition temperatures.

in.

Figure 4 presents a series of dense magnetization curves measured along the easy b -axis. For the sake of straightforward comparison with the afore-discussed susceptibility data, these experiments were focused on magnetic fields lower than 2 T and temperatures close to $T_{N,t}$. As seen, the "devilish" field dependence of the magnetization, observed at 1.7 K [Fig. 2(c)], is hardly visible at temperatures higher than 4.4 K. However, upon decreasing T a sequence of distinct steps in the $M(B)$ curve emerges from the smooth curve. Three of these steps, located at 3.8 K at about 0.15, 0.32 and 0.53 T, dominate the magnetization, yet several less visible anomalies can also be found on the $M(B)$ curve. The experimental data displayed on Figs. 3 and 4 were used for constructing a tentative phase diagram described in Sec. IV.

C. Electrical resistivity

Figure 5 presents the electrical resistivity of single-crystalline CeRh_3Si_2 as a function of temperature, measured with the current i flowing along the main crystallographic directions. Clearly, the compound exhibits good metallic conductivity in the entire temperature range studied. The antiferromagnetic phase transition manifests itself as a drop in $\rho(T)$ at about

4.7 K, being equal to the Néel temperature deduced from the magnetic measurements performed in the weakest magnetic fields (cf. Fig. 3). Closer look at the low-temperature range [see the inset to Fig. 5] unambiguously shows the presence of another kink on the $\rho(T)$ curve that occurs at about 4.5 K. The latter finding is in-line with the scenario of two subsequent magnetic phase transitions discussed in Sec. III B.

As can be inferred from Fig. 5, the resistivity measured along the a -axis is much smaller than ρ taken along the b - and c -axes. At 300 K, the ratio $\rho_b/\rho_a \approx \rho_c/\rho_a \cong 4$. Moreover, the anomalies at T_N and T_t are hardly visible on the $\rho_a(T)$ curve. This behavior is fully consistent with the established for CeRh_3Si_2 very large magnetocrystalline anisotropy, characterized by the magnetic moments confined to the bc plane.

Our several attempts to measure the resistivity of polycrystalline LaRh_3Si_2 failed because of multitude of microcracks present in the specimens. For this reason it was not possible to extract the magnetic contribution to the electrical resistivity of CeRh_3Si_2 employing a commonly used method of subtracting the resistivity of its non-magnetic counterpart.

D. Specific heat

Figure 6 displays the temperature dependencies of the specific heat of CeRh_3Si_2 and its non-magnetic isostructural counterpart LaRh_3Si_2 . At low temperatures a distinct anomaly located at about 4.7 K confirms the antiferromagnetic ordering of the cerium moments in CeRh_3Si_2 . The overall shape of $C(T)$ obtained for the La-based compound is in turn typical for non-magnetic metals. In particular, below about 7 K it is easily describable by the formula:

$$C(T) = \gamma T + \frac{12\pi^4 nR}{5 \Theta_D^3} T^3, \quad (1)$$

in which the first term is a conventional conduction-electron contribution to the specific heat with γ being the Sommerfeld coefficient, and the second term is a low-temperature phonon contribution in a form of the Debye- T^3 law with the characteristic Debye temperature Θ_D , the universal gas constant R , and n being a number of atoms in the formula unit [34]. Least-squares fitting of Eq. (1) to the experimental data (see the solid line in the inset to Fig. 6) yielded the values of $\gamma = 3 \text{ mJ}/(\text{mol K}^2)$ and $\Theta_D = 428 \text{ K}$. At higher temperatures

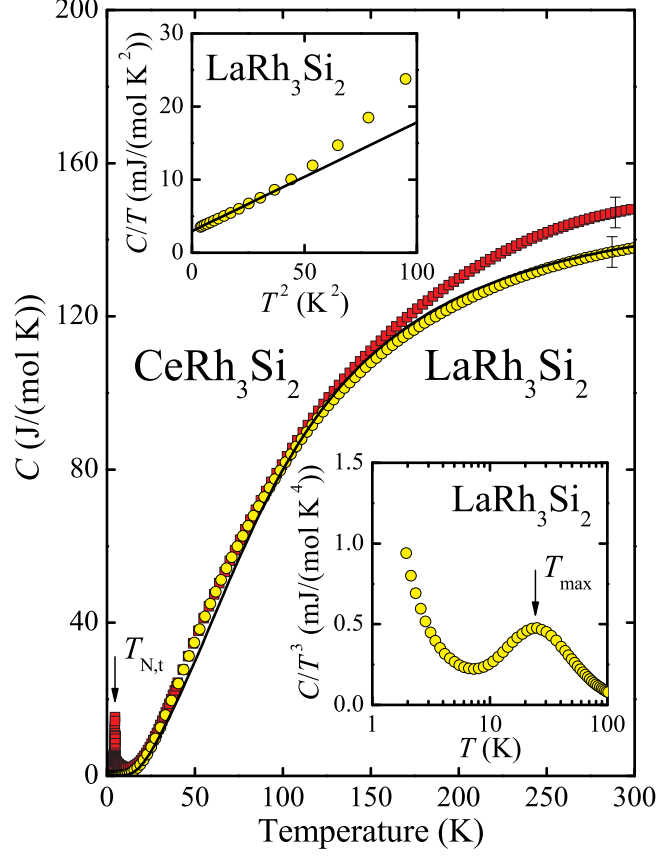


FIG. 6: (Color online) (a) Specific heat of single-crystalline CeRh_3Si_2 (squares) and polycrystalline LaRh_3Si_2 (circles) as a function of temperature; the solid line is a fit of Eq. (2) to the experimental data, the arrow marks the Néel temperature. The upper inset shows C/T vs. T^2 measured for the La-based compound; the straight solid line is a fit of the Debye T^3 -law [Eq. (1)]. The lower inset displays the specific heat of LaRh_3Si_2 divided by T^3 as a function of T ; the arrow marks the position of a maximum (for its interpretation see the text).

$C(T)$ of LaRh_3Si_2 can be described by the equation:

$$C(T) = \gamma T + n_D \times 9R \left(\frac{T}{\Theta_D} \right)^3 \int_0^{\Theta_D/T} \frac{x^4 e^x}{(e^x - 1)^2} dx + n_E \times 3R \left(\frac{\Theta_E}{T} \right)^2 \frac{e^{\Theta_E/T}}{(e^{\Theta_E/T} - 1)^2}, \quad (2)$$

in which the second term is the full Debye expression for the phonon specific heat, and the third term describes the phonon specific heat within the Einstein model of lattice vibrations (see e.g. Refs. [34,35]) with Θ_E being the characteristic Einstein temperature. The coefficients n_D and n_E are numbers of atoms in the formula unit ($n_D + n_E \equiv n$), vibration of which were assumed to follow the Debye or Einstein models, respectively. The solid line in Fig. 6 presents the temperature variation of the specific heat calculated employing Eq. (2) with the

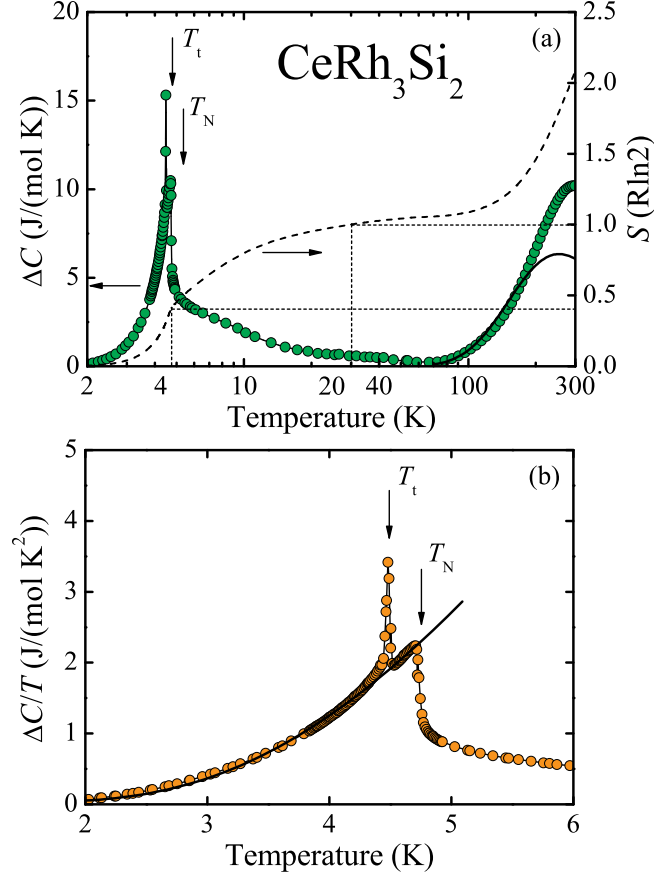


FIG. 7: (Color online) (a) Logarithmic temperature variation of the magnetic contribution to the specific heat of CeRh₃Si₂ (left axis); the thin solid curve serves as a guide for the eye, the arrows mark the magnetic transition temperatures, and the thick solid line represents the Schottky contribution calculated for the CEF level scheme from Tab. IV. The dashed curve is the magnetic entropy S of the compound (right axis); the drop lines mark the values of $S(T_N)$ and $T(S = R \ln 2)$. (b) $\Delta C/T$ at low temperatures; the solid curve is a fit of Eq. (3) to the experimental data in the magnetically ordered region, and the arrows mark the magnetic transition temperatures.

parameters $\gamma = 3$ mJ/(mol K²) and $\Theta_D = 428$ K (as determined from the low-temperature data), and $\Theta_E = 125$ K, $n_D = 5$ and $n_E = 1$. The two latter values (n_D and n_E) were chosen arbitrarily, assuming that the rare-earth atoms (1/f.u.) in CeRh₃Si₂ and LaRh₃Si₂, which occupy the centers of the hexagonal tubes (see Fig. 1 and Sec. III A), are weakly coupled with their surroundings (5 at./f.u.) and exhibit some tendency to vibrate independently of the whole lattice. The characteristic temperature of those vibrations (i.e. the Einstein temperature) was estimated on the basis of simple analysis of $C(T)$ measured for the La-

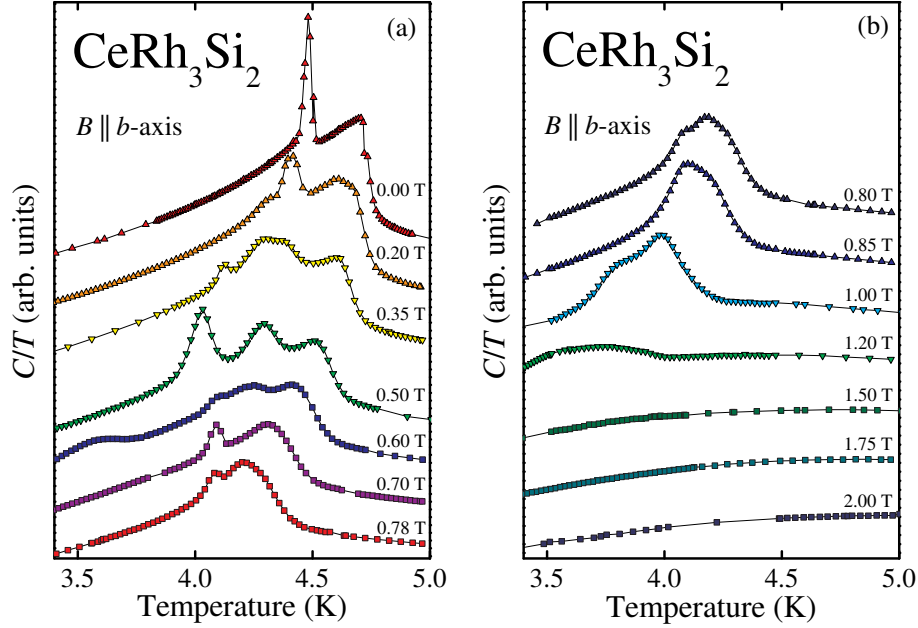


FIG. 8: (Color online) Specific heat of single-crystalline CeRh_3Si_2 measured at low temperatures in several different magnetic fields B applied along the b -axis. The curves are shifted up for the sake of clarity.

based compound: analytical properties of the Debye and Einstein functions allow to relate the position T_{max} of the low-temperature maximum in the $C(T)/T^3$ curve to the Einstein temperature as $\Theta_E \approx 5 \times T_{\text{max}}$. In the case of LaRh_3Si_2 $T_{\text{max}} \approx 25$ K, hence $\Theta_E \approx 125$ K (see the lower inset to Fig. 6).

In order to estimate a $4f$ -derived contribution $\Delta C(T)$ to the total heat capacity of CeRh_3Si_2 , the phonon specific heat of LaRh_3Si_2 was subtracted from $C(T)$ of the Ce-based compound. As apparent from Fig. 7(a), the so-obtained $\Delta C(T)$ exhibits in the paramagnetic region a distinct Schottky-like anomaly due to CEF effect. The thick solid line in Fig. 7(a) represents the Schottky specific heat calculated for the CEF model derived in Sec. III E. Apparently, the model accounts reasonably well for the experimental data, except for high temperature region, where significant quantitative discrepancy is seen. The shortcomings likely arise because of the accumulation of experimental errors (see Fig. 6) directly influencing reliability of the subtraction procedure.

Below about 50 K, the magnetic contribution to the specific heat of CeRh_3Si_2 increases again, and at about 4.70(1) K $\Delta C(T)$ takes a form of distinct λ -shaped anomaly, followed by another pronounced peak, that occurs at about 4.48(1) K. While the λ -shaped feature

corresponds to the second-order antiferromagnetic phase transition evidenced at T_N in the magnetic susceptibility data, the second feature can be ascribed to the spin-rearrangement at T_t . The characteristic spike-like shape of that singularity is typical for first order phase transitions. In turn, the magnetic contribution to the specific heat in the range 5–50 K can be attributed to short-range interactions, which evolve finally into the long-range antiferromagnetic ordering. The latter hypothesis is supported by the temperature dependence of the magnetic entropy, defined as $S(T) = \int_0^T \Delta C(T)/T dT$. As can be inferred from Fig. 7(a) (right axis), the entropy at T_N is strongly reduced in comparison to the entropy of the ground state doublet ($= R \ln 2$) and amounts only to about $0.44 R \ln 2$. The value of $R \ln 2$ is achieved at temperature as high as ≈ 30 K, suggesting that even well above T_N the system is not yet completely disordered.

In the ordered region, the specific heat of CeRh_3Si_2 is dominated by an antiferromagnetic magnon contribution. Assuming that the dispersion relation in the antiferromagnetic spin-wave spectrum has a relativistic form $\omega = \sqrt{\Delta^2 + D^2 k^2}$ (where ω , D and k are the spin-wave frequency, stiffness, and wave number, respectively, and Δ is a spin-wave gap) $\Delta C(T)$ takes the form of a sum of the electronic and magnon contributions [36]:

$$\Delta C(T) = \gamma T + A \Delta^4 \sqrt{\frac{T}{\Delta}} e^{-\Delta/T} \left[1 + \frac{39}{20} \left(\frac{\Delta}{T} \right) + \frac{51}{32} \left(\frac{\Delta}{T} \right)^2 \right], \quad (3)$$

where A is a proportionality coefficient related to D as $A \propto 1/D^3$. Least-squares fitting procedure [see the solid line in Fig. 7(b)] yielded the values: $\gamma = 7$ mJ/(mol K²), $A = 3$ mJ/(mol K⁴), and $\Delta = 16$ K. The small value of the Sommerfeld coefficient, which can be also directly deduced from Fig. 7(b) as $\Delta C(T)/T|_{T \rightarrow 0}$, is typical for simple metals.

Figure 8 shows the results of the specific heat measurements done in several different magnetic fields applied parallel to the b -axis. As in the case of the magnetization measurements the latter experiments were also focused on the temperature region close to T_N and T_t . As seen, the two anomalies visible in zero magnetic field at 4.7 and 4.5 K split in higher fields into four separate features in $C(T)/T$, which independently shift to lower temperatures with rising B . However, all of the anomalies systematically broaden and in $B \geq 0.7$ T one can distinguish only two of them. Finally, in $B = 1.2$ T only one hump at about 3.7 K is visible, and in $B \geq 1.5$ T the specific heat curve is featureless. The positions of the anomalies from Fig. 8 served as complementary set of data used for constructing the tentative phase diagram shown Sec. IV.

TABLE IV: CEF parameters, molecular field constant λ , eigenenergies and eigenwavefunctions obtained from the fitting of the experimental magnetic susceptibility data and the Schottky contribution to the specific heat.

Parameter	Value [K]
B_{20}	1322
B_{22}	-1265
B_{40}	727
B_{42}	1327
B_{44}	-2345
B_{60}	-7478
B_{62}	-2197
B_{64}	3060
B_{66}	22239
λ [mol m ⁻³]	501176
SQX	1.86%
Eigenvalues [K]	Eigenvectors
0	$-0.801 5/2, 5/2\rangle + 0.428 5/2, 1/2\rangle - 0.407 5/2, -3/2\rangle$
655	$0.875 5/2, 3/2\rangle - 0.289 5/2, -5/2\rangle - 0.255 7/2, 3/2\rangle + \dots$ $\dots + 0.239 5/2, -1/2\rangle - 0.126 7/2, -1/2\rangle$
692	$-0.783 5/2, 1/2\rangle - 0.464 5/2, 5/2\rangle - 0.334 7/2, 1/2\rangle + 0.223 7/2, -7/2\rangle$
3091	$-0.765 7/2, 7/2\rangle - 0.511 7/2, -1/2\rangle + 0.313 7/2, 3/2\rangle - 0.235 7/2, -5/2\rangle$
3478	$-0.940 7/2, 5/2\rangle + 0.246 7/2, 1/2\rangle - 0.217 7/2, -3/2\rangle$
5467	$-0.742 7/2, -1/2\rangle + 0.459 7/2, 7/2\rangle - 0.232 7/2, 3/2\rangle + \dots$ $\dots - 0.381 5/2, -1/2\rangle - 0.138 7/2, -5/2\rangle - 0.133 5/2, -5/2\rangle$
5882	$-0.854 7/2, 3/2\rangle - 0.383 7/2, 7/2\rangle - 0.233 5/2, 3/2\rangle + \dots$ $\dots + 0.202 5/2, -5/2\rangle + 0.170 7/2, -5/2\rangle$

E. CEF calculations

The temperature dependence of the magnetic susceptibility (Sec. III B) and the Schottky contribution to the heat capacity (Sec. III D) of CeRh₃Si₂ suggest predominantly localized

character of the f -electrons and the importance of definite sequence of the CEF levels. To capture the main features of the $4f^1$ state split in the CEF potential, we apply here the standard static description based on the renormalized Hamiltonian projected on the space of the pure f -electron states. The approach is known to be quite satisfactory for insulating systems, strongly supported by both qualitative and quantitative theoretical studies [37,38].

In the Wybourne notation [39], the one-electron CEF potential of the C_{2v} point symmetry appropriate to the case of $CeRh_3Si_2$ reads :

$$H_{\text{CEF}} = B_{20}\hat{C}_0^{(2)} + B_{22}\hat{C}_2^{(2)} + B_{40}\hat{C}_0^{(4)} + B_{42}\hat{C}_2^{(4)} + B_{44}\hat{C}_4^{(4)} + B_{60}\hat{C}_0^{(6)} + B_{62}\hat{C}_2^{(6)} + B_{64}\hat{C}_4^{(6)} + B_{66}\hat{C}_6^{(6)}. \quad (4)$$

where B_{kq} are the CEF parameters, which are to be adjusted to the experimental data and $\hat{C}_q^{(k)}$ are the normalized spherical harmonics. Besides, we employ also a simplified, angular-overlap-model (AOM) form of the CEF potential defined through matrix elements of the effective CEF interaction (see for instance Ref. 38):

$$\langle m | H_{\text{CEF}} | m' \rangle = \sum_{\tau t} \sum_{\mu} D_{\mu m}^{(3)*}(0, \Theta_{\tau t}, \Phi_{\tau t}) D_{\mu m'}^{(3)}(0, \Theta_{\tau t}, \Phi_{\tau t}) e_{\mu}^{\tau}. \quad (5)$$

In this equation, $D_{\mu m}^{(3)}(0, \Theta_{\tau t}, \Phi_{\tau t})$ is the matrix element of the irreducible representation $D^{(3)}$ of the rotation group, and $R_{\tau t}, \Theta_{\tau t}, \Phi_{\tau t}$ are the angular coordinates of the nearest neighbor atom τt expressed in the coordination system set at the magnetic atom site. The index τ distinguishes various chemically nonequivalent atoms and t runs over nearest neighbors τ atoms. Thus, the whole CEF effect is described by three intrinsic parameters e_{μ}^{τ} with $\mu = 0(\sigma), 1(\pi), 2(\delta)$ for each chemically nonequivalent nearest neighbor atom τ . In the present case there are six silicon atoms and six rhodium atoms in the coordination sphere of the radius of 3.34 Å. This coordination implies six non-equivalent AOM parameters, three for each nearest neighbor atom. If we neglect e_{δ} and/or tie up e_{π} with one third of e_{σ} (following the rules observed for insulating systems [37]), four-parameters or two-parameters versions of AOM can be applied.

The Hamiltonian H includes also the spin-orbit interaction:

$$H_{\text{SO}} = \zeta_{4f} \mathbf{l} \cdot \mathbf{s} \quad (6)$$

with the spin-orbit constant ζ_{4f} equal to 647.3 cm^{-1} (931.4 K) [40], and the Zeeman term:

$$H_{\text{M}} = \mu_{\text{B}} \left[(l_x + 2s_x) \frac{B_x}{B} + (l_y + 2s_y) \frac{B_y}{B} + (l_z + 2s_z) \frac{B_z}{B} \right] B \quad (7)$$

describing the system response to the external magnetic field B :

$$H = H_{\text{CEF}} + H_{\text{SO}} + H_{\text{M}} \quad (8)$$

Following Refs. 41 and 42, the molar magnetization $M_{\text{mol},\alpha}$ and the magnetic susceptibility χ_α are calculated from derivative of the free energy F of the system:

$$F = -\frac{N}{\beta} \sum_{\nu} \exp(-\beta E_{\nu}); \beta = 1/(k_{\text{B}}T) \quad (9)$$

with respect to the magnetic field direction α , *i.e.*:

$$M_{\text{mol},\alpha} = -\frac{1}{V} \frac{\partial F}{\partial B} = N_{\text{A}} \frac{\sum_{\nu} \mu_{\nu,\alpha} \exp(-\beta E_{\nu,\alpha})}{\sum_{\nu} \exp(-\beta E_{\nu,\alpha})} \quad (10)$$

where

$$\mu_{\nu,\alpha} = -\frac{\partial E_{\nu,\alpha}}{\partial B} \quad (11)$$

and $E_{\nu,\alpha}$ are the eigenenergies of the Hamiltonian given by Eq. 8. The molar susceptibility is defined as:

$$\chi_\alpha = \mu_0 \frac{M_{\text{mol},\alpha}}{B}. \quad (12)$$

The CEF parameters in Eq. 4 have been fitted to restore the temperature dependences of the magnetic susceptibility measured along the a -, b - and c - axes and simultaneously account for the Schottky contribution to the heat capacity (see section III D). For this purpose the Levenberg-Marquardt method [43] was applied in the version implemented in the computer programs by Helmut Schilder and Heiko Lueken [41,42,44,45]. In order to scan the entire parametric space, several initial CEF parameter sets have been probed. Among them one may distinguish three special cases: (i) zero-values, (ii) the CEF parameters reported for the compound CeIr_3Si_2 [46] and (iii) the parameters estimated using AOM with the values: $e_\sigma^{Si} = -300, 300, 600 \text{ cm}^{-1}$ ($-432, 432, 864 \text{ K}$), $e_\pi^{Si} = \pm \frac{1}{3} e_\sigma^{Si}$, $e_\delta^{Si} = -100, 0, 100 \text{ cm}^{-1}$ ($-144, 0, 144 \text{ K}$) and $e_\sigma^{Rh} = -200, 200 \text{ cm}^{-1}$ ($-288, 288 \text{ K}$), $e_\pi^{Rh} = \pm \frac{1}{2} e_\sigma^{Rh}$, $e_\delta^{Rh} = -50, 0, 50 \text{ cm}^{-1}$ ($-72, 0, 72 \text{ K}$). Besides, several independent initial randomly generated CEF parameters sets (over 230) have been probed as well.

The fitting procedure was same for each of the initial CEF parameters set. First, we fit the two second-order parameters, whereas the remaining ones were kept at their initial values. Then, the parameters of second and sixth rank were fixed at their values determined in the previous step, while the fourth-rank parameters were fit. Subsequently, all the second-rank and the fourth-rank parameters were varied simultaneously. In the following we call

this initial step the base phase, in which the general shapes of the experimental magnetic susceptibility curves have been reproduced fairly well, yet some details of the measured curves could not be accounted for.

In the second, refining, phase we included the sixth-rank CEF parameters. Their influence on the thermal properties is expected to be of less significance, as they only determine the CEF admixture of the $7/2$ states having energies above 2000 cm^{-1} (2878 K) to the low-energy $5/2$ states predominantly governing the thermodynamic properties of the compound studied in moderate temperature ranges. This admixture modifies rather slightly both the CEF splitting of the $5/2$ state and the matrix elements of the angular momentum operator. Nevertheless, the mixing may become more pronounced if the CEF effect is strong enough. Indeed, some preliminary simulations showed that in the case of CeRh_3Si_2 the admixture of the $j = 7/2$ states may reach as much as 10% for the lowest states. Hence, we decided to include the sixth-rank states in the refining phase, and as a result the relative root mean square error SQX [44,47,48] has dropped from 2.92% to 1.86%.

The fitting procedure of the sixth-order parameters were analogous to that of the fourth order. First, we varied only the sixth-order parameters, while keeping all the remaining parameters fixed on the values determined in the base phase. In the final step all the CEF parameters were varied simultaneously. In each step the molecular field constant λ was also varied.

Most of the probed initial sets of CEF parameters led to stable solutions of three different types. The corresponding fits yielded similar sequences of the CEF levels but distinctly different parameters sets, except for the two second-rank parameters, which appeared to have fairly similar values in each solution. The best fitting results are collected in Tab. IV. As seen from this table, the CEF effect is generally large and leads to the total splitting of the $5/2$ state of the order of 500 cm^{-1} (720 K) and the overall $4f^1$ splitting exceeding 4000 cm^{-1} (5755 K). Despite the pronounced differences between the parameters in the three distinct sets (only the solution giving lowest SQX is shown) the sequence of levels and the model curves are almost same, what is reflected in negligible differences in the root-square errors and the energies. The scattering of some fourth- and especially sixth-rank CEF parameters in various solutions confirms rather limited reliability of the latter parameters. Consequently, as the final result we accepted the solution characterized by the lowest root-square error. The so-obtained model curves are shown in Fig. 2 together with

the experimental ones. Additionally, Fig. 7(a) presents the calculated Schottky contribution expected for the obtained CEF splitting scheme.

F. X-ray photoemission spectroscopy

Analysis of the Ce $3d$ XPS spectra is a proper method to investigate the character of the Ce $4f$ states in Ce-intermetallic compounds due to the strong Coulomb interaction between photoemission holes in the $3d$ shell and electrons located near the Fermi level. $3d$ core ionization of Ce-based compounds usually results in a spectrum of final states, whose configurations correspond to the f^0 , f^1 , and f^2 states (see Refs. 49 and 50).

Figure 9(a) shows the Ce $3d$ XPS spectrum obtained for CeRh₃Si₂. Two final-state contributions f^1 and f^2 are clearly observed, which exhibit spin-orbit splitting $\Delta_{SO} \cong 18.6$ eV. In turn, the f^0 component is not evident in the spectrum, which implies stable valence 3+ of the cerium atoms. According to the Gunnarsson and Schönhammer theory [49], the hybridization energy Δ_{fs} , which describes the hybridization part of the Anderson impurity Hamiltonian [51] and is defined as $\pi V^2 \tilde{\rho}_{max}$ [where $\tilde{\rho}_{max}$ is the maximum in the density of states (DOS) and V is the hybridization matrix element], can be estimated from the ratio $r = I(f^2)/(I(f^1)+I(f^2))$ of the $I(f^2)$ and $I(f^1)$ intensities [50]. The particular contributions to the $3d$ XPS spectrum can be derived by its analysis in terms of the Doniach-Šunjić approach [52] (the experimental details and accuracy of the method is also discussed in Ref. 53). This way, for CeRh₃Si₂ one estimates a hybridization width Δ_{fs} of ~ 56 meV.

More evidence for the stable valence of Ce³⁺ ions in CeRh₃Si₂ comes from the Ce $4d$ XPS spectrum displayed in Fig. 9(b). Clearly, there is no additional peak at higher binding energies ($E > 118$ eV) that could be attributed to the Ce $3d^9 f^0$ state [50,54,55].

G. Electronic band structure calculations

The band structure calculations were performed using the Wien2k code within the LDA, LDA+U and LSDA+OP schemes [the first two approaches with (LSDA and LSDA+U) and without spin polarization]. Non spin polarized densities of electronic states were used for calculations of photoemission spectra, which in experiment were measured at room temperature, well above $T_N=4.72$ K. In the case of spin polarized calculations the antiferromagnetic

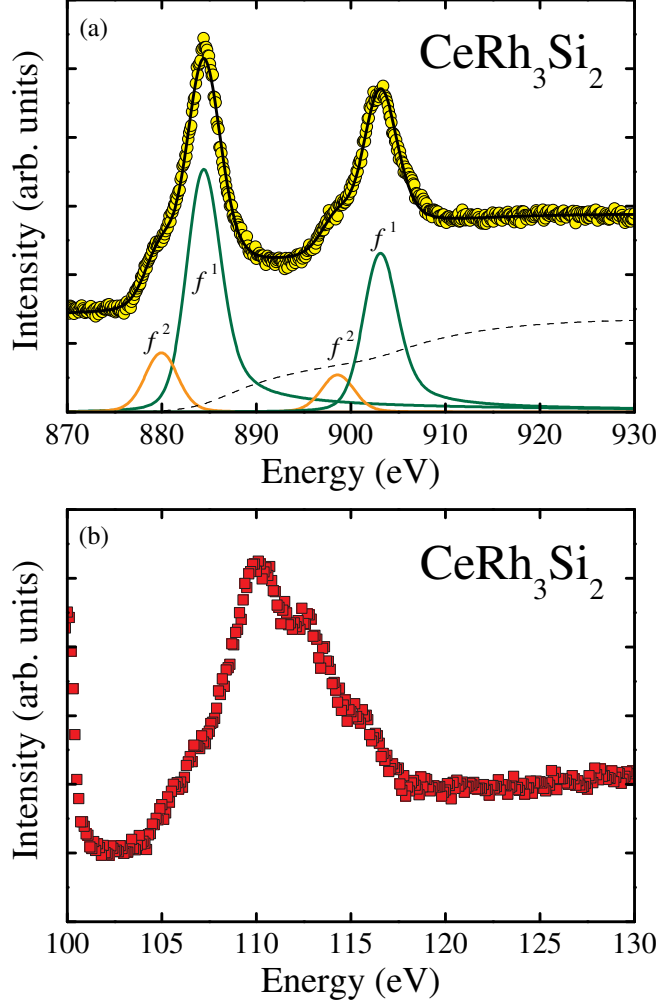


FIG. 9: (color online) (a) Ce 3d and (b) Ce 4d XPS spectra obtained for CeRh_3Si_2 . The f^1 and f^2 components were separated on the basis of the Doniach-Šunjić theory.

solution was not assumed in advance. The twelve atoms forming unit cell that was used in our calculations were treated as different types of atoms. The starting magnetic moments were chosen to have opposite sign. The system reached, iteration by iteration, a selfconsistent solution that was very close to the antiferromagnetic state. The resultant magnetization of both sublattices was almost balanced and was equal to about $2 \times 10^{-3} \mu_B$ per f.u..

In the first step of our calculations, we employed the LSDA approach. The calculated densities of states (DOS) for CeRh_3Si_2 system are presented in Fig.10: (a) the total DOS and (b) the contributions provided by 4f electrons located on cerium atoms forming two magnetic sublattices. The valence band can be divided into two parts below the Fermi level (E_F), here located at $E=0$. The first part located in the range of $(-11.5;-7.5)$ eV is

formed mainly by electrons provided by silicon atoms Si(3s). The main part of the valence band between about -7.5 eV and E_F is created by Rh(4d) and Si(3p) electrons. The Ce(4f) electrons provide contribution nearest the Fermi level, and they have the main contribution to DOS at $E=E_F$: 5.43 states/(eV atom), 77.5% of the total value 7.01 states/(eV f.u.).

Based on DOS at E_F one can calculate the Sommerfeld coefficient γ_0 , which in our case is equal to about 16.5 mJ/(mol K²). This value is much higher than the experimental one $\gamma_{exp}=3$ mJ/(mol K²), reported earlier in Sec. IIID. This discrepancy is probably caused by inadequate description of the strongly correlated 4f electrons by the LSDA formalism.

Hybridization changes initial configuration $6s^25d^14f^1$ to the final one $6s^{1.99}5d^{0.57}4f^{1.02}$. Total number of electrons is different from those for pure cerium systems because of charge transfer from/to rhodium and silicon atoms as well as the charge accumulated in the interstitial region between atomic spheres.

The values of site projected moments on cerium atoms are equal to $\pm 0.08 \mu_B$ per Ce atom. The resultant value is not spectacular because of opposite alignment of spin and orbital moments. Until now the experimental values of local moments were not known.

The shape of DOS obtained by LSDA+OP approach (Fig. 10 (c) and (d)) is similar to that reported earlier but usually in this approach the magnetic moments increase, in our case to $\pm 0.5 \mu_B$ per Ce atom. Unfortunately the DOS at E_F is still too high: 10.65 states/(eV f.u.) with contribution of 4f electrons of about 8.52 states/(eV Ce atom). The Sommerfeld coefficient is equal to 25.1 mJ/(mol K²).

On the two lowest panels of Fig. 10 we present results of LSDA+U approach with U equal to 6 eV. The additional U term to the LSDA approach shifts the 4f DOS (in LSDA located well below E_F) towards higher binding energies (now located around -2 eV). The unoccupied part of 4f DOS is moved to the energies about 4 eV above the Fermi level. In this way the contribution of Ce(4f) electrons to the DOS at E_F is practically negligible, and the Fermi level is located in a pseudo gap of the DOS. The value of $DOS(E_F)=1.01$ states/(eV f.u.) gives the Sommerfeld coefficient equal to 2.39 mJ/(mol K²). The latter value is slightly smaller than the experimental Sommerfeld coefficient as it should be for theory. The magnetic moments are equal to $\pm 0.09 \mu_B$ per Ce atom.

Figure 11 presents experimental and calculated X-ray photoelectron spectra based on non spin polarized DOS plots and calculated cross sections collected in Ref. 28. The best fitting to the experimental photoemission spectrum was obtained for the LDA calculations. The

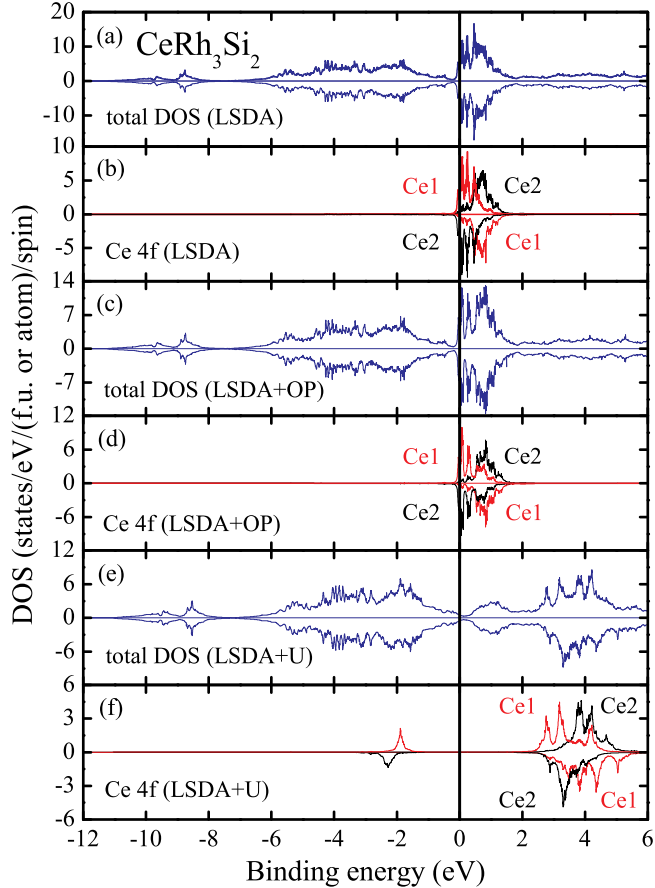


FIG. 10: The total (per f.u.) and site projected (per Ce atom) densities of electronic states (DOS) for antiferromagnetic CeRh_3Si_2 calculated within the LSDA, LSDA+OP, and LSDA+U schemes.

consistency between the calculated and experimental spectra is quite good. The spectrum is dominated by the Rh(4d) electrons. The Ce(4f) electrons provide contributions near the Fermi level. The peak located at about 8-9 eV below E_F is formed mainly by the Si(3s) electrons (not shown here).

IV. SUMMARY

CeRh_3Si_2 was found to crystallize in the orthorhombic ErRh_3Si_2 -type structure with honey-comb-like Rh-Si cages surrounding the Ce ions, which occupy just one inequivalent crystallographic position in the unit cell. The 4f electrons are well localized and experience exceptionally strong (as for cerium intermetallics) crystalline-electric-field effect with significant admixture of two j -multiplets (i.e. 5/2 and 7/2). In the whole temperature range

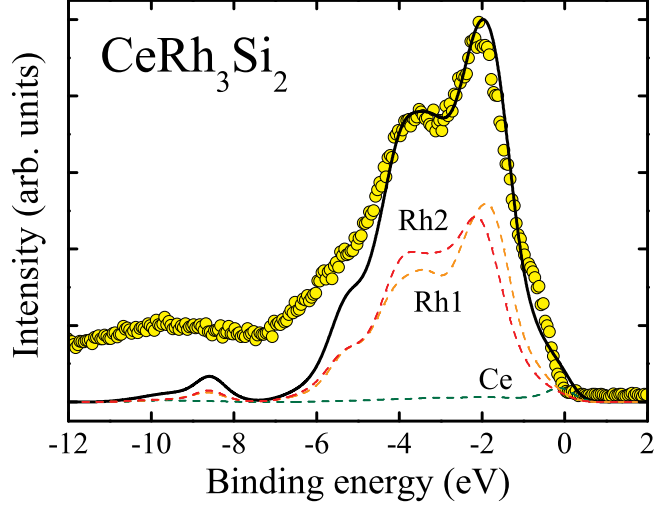


FIG. 11: The measured X-ray photoelectron spectrum for the valence band compared with the calculated ones within the LDA approach for CeRh_3Si_2 system.

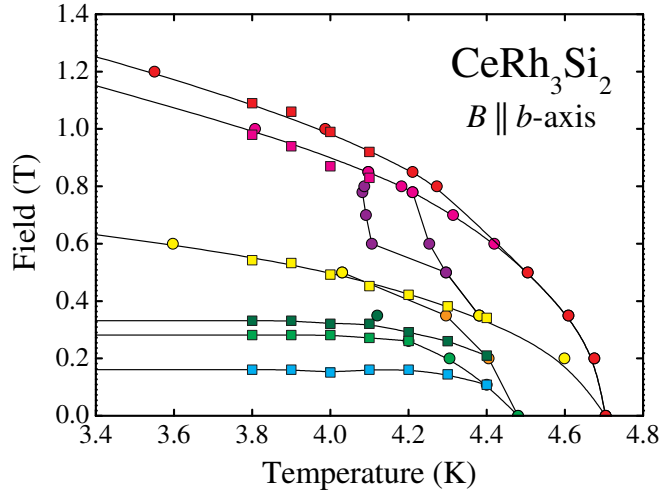


FIG. 12: (Color online) Tentative $B-T$ phase diagram for single-crystalline CeRh_3Si_2 based on anomalies observed in temperature dependencies of magnetic susceptibility (squares; Fig. 3), field variations of magnetization (squares; Fig. 4) and the temperature dependencies of the specific heat (circles; Fig. 8) for $B \parallel b$ -axis. Solid curves are hypothetical phase-boundary lines. Colors serves as a guide for the eye.

covered CeRh_3Si_2 exhibits very large easy ab plane anisotropy in its magnetic and electrical transport behavior. At low temperatures the compound undergoes two subsequent anti-ferromagnetic phase transitions. The experiments performed in external magnetic fields B

applied parallel to the easy b -axis revealed very complex $B - T$ phase diagram of CeRh_3Si_2 (Fig. 12), which needs to be verified by neutron-scattering studies. The band structure calculations confirmed the antiferromagnetic ordering of the cerium magnetic moments. The calculated values of these moments are equal to 0.08, 0.09, and $0.5 \mu_B$ per Ce atom for the LSDA, LSDA+U, and LSDA+OP approach, respectively. Only LSDA+U calculations yielded correct relation between theoretical [$2.39 \text{ mJ}/(\text{mol K}^2)$] and measured [$3 \text{ mJ}/(\text{mol K}^2)$] values of the Sommerfeld coefficients being less than one. The non-spin-polarized DOS plots reproduced well the experimental X-ray photoelectron spectrum of the valence band.

It is worth noting that properties similar to those of CeRh_3Si_2 (i.e. "devilish" magnetization, complex magnetic phase diagram, strong CEF effect) were reported for a number of magnetically ordered rare-earth intermetallics. Among them one can mention highly anisotropic CeIr_3Si_2 [46], TbNi_2Ge_2 [33,56], TbNi_2Si_2 [32] and CeSb [30,31]. All these compounds exhibit several successive field-induced metamagnetic phase transitions, which manifest themselves as a series of sudden jumps between well-defined plateaus of field-dependent magnetization. Detailed bulk direction-dependent physical properties measurements as well as neutron diffraction and x-ray resonant exchange scattering studies have revealed that in all of these compounds one deals with non-trivial field-induced spin rearrangements. In most cases the metamagnetic processes are relatively well understood and described phenomenologically, yet microscopic models were proposed only for a limited number of the systems (for survey see Ref. 57 and references therein). In most cases, the magnetic behavior was interpreted in terms of the Ising model with next-nearest neighbour interactions (Axial Next-Nearest Neighbor Ising model, ANNNI), which (in an ideal case) can produce an infinite number of commensurate phases occurring with an infinite number of steps in field-dependent magnetization, called commonly a "devil's staircase" (for review see *e.g.* Ref. 58). Other theoretical approaches were proposed for TmAgGe [59] and $\text{HoNi}_2\text{B}_2\text{C}$ [60]. The former compound has been found to exhibit some features of frustrated system with distorted antiferromagnetic Kagome-like layered structure. The sequence of field-induced metamagnetic transitions observed in the compound TmAgGe was successfully reproduced using a hamiltonian that describes only (i) relatively weak antiferromagnetic next-nearest-neighbor and ferromagnetic nearest-neighbor exchange adopted to the geometry of the system, and (ii) strong crystal electric field effect [61]. In turn, $\text{HoNi}_2\text{B}_2\text{C}$ is a magnetically ordered superconductor, which shows at low-temperatures a transition from commensurate

antiferromagnetic to incommensurate c -axis complex spiral state with some a -axis incommensurate modulation (see Refs. 62–64 and references therein). Here again the crystalline electric field was taken into account to explain the complex magnetic phase diagram [65], yet the generalized ANNNI model (a kind of so-called clock model) was also successfully applied [66].

The microscopic origin of the complex magnetic behavior of CeRh_3Si_2 cannot be defined at this stage of our study. The most relevant factor governing its strongly anisotropic properties in the ordered and paramagnetic states is clearly unusually strong crystalline electric field potential that yield the total splitting of the $5/2$ state of about 720 K and the overall $4f^1$ splitting as large as about 5760 K. The estimated magnitude of the CEF effect in CeRh_3Si_2 is perhaps the largest ever reported for Ce-based intermetallics. The other cerium compounds known for their giant CEF interactions are CeRh_3B_2 [67,68] and CeIr_3Si_2 [46], where the total CEF splitting is about 2000 K and 1600 K, respectively. Remarkably, the latter compound is isostructural to CeRh_3Si_2 , while the crystal structure of CeRh_3B_2 is closely related to that of CeRh_3Si_2 . Further studies, including inelastic neutron scattering experiments and ANNNI calculations, are needed to shed more light on the unique features (i.e. unusually strong CEF and complex magnetic behavior) of the latter compound.

Acknowledgments

We are grateful to Dr. Helmut Schilder for developing his computer program towards simultaneous fitting of the heat capacity and for the engagement and support. This work was supported by the Ministry of Science and Higher Education within grants no. N202 116 32/3270 and N202 1349 33. Part of the research was performed in the frame of the National Network "Strongly correlated materials: preparation, fundamental research and applications".

¹ A. Lipatov, A. Griбанov, A. Grytsiv, S. Safronov, P. Rogl, J. Rousnyak, Y. Seropegin, and G. Giester, *J. Solid State Chem.* **183**, 829 (2010).

² D. T. Adroja and B. D. Rainford, *J. Magn. Magn. Mater.* **119**, 54 (1993).

- ³ C. Godart, C. V. Tomy, L. C. Gupta, and R. Vijayaraghavan, *Solid State Commun.* **67**, 677 (1988).
- ⁴ D. Kaczorowski, A. Pikul, U. Burkhardt, M. Schmidt, A. Ślebarski, A. Szajek, M. Werwiński, and Y. Grin, submitted to *Phys. Rev. B*.
- ⁵ D. Kaczorowski, Y. Prots, U. Burkhardt, and Y. Grin, *Intermetallics* **15**, 225 (2007).
- ⁶ R. Settai, A. Misawa, S. Araki, M. Kosaki, K. Sugiyama, T. Takeuchi, K. Kindo, Y. Haga, E. Yamamoto, and Y. Onuki, *J. Phys. Soc. Jpn.* **66**, 2260 (1997).
- ⁷ Y. Muro, D. Eom, N. Takeda, and M. Ishikawa, *J. Phys. Soc. Jpn.* **67**, 3601 (1998).
- ⁸ S. Araki, M. Nakashima, R. Settai, T. C. Kobayashi, and Y. Onuki, *J. Phys.: Condens. Matter* **14**, L377 (2002).
- ⁹ R. Movshovich, T. Graf, D. Mandrus, J. D. Thompson, J. L. Smith, and Z. Fisk, *Phys. Rev. B* **53**, 8241 (1996).
- ¹⁰ N. Kimura, K. Ito, K. Saitoh, Y. Umeda, H. Aoki, and T. Terashima, *Phys. Rev. Lett.* **95**, 247004 (2005).
- ¹¹ N. Kimura, Y. Muro, and H. Aoki, *J. Phys. Soc. Jpn.* **76**, 051010 (2007).
- ¹² A. V. Morozkin and Y. D. Seropegin, *J. Alloys Compd.* **237**, 124 (1996).
- ¹³ T. Graf, M. F. Hundley, R. Modler, R. Movshovich, J. D. Thompson, D. Mandrus, R. A. Fisher, and N. E. Phillips, *Phys. Rev. B* **57**, 7442 (1998).
- ¹⁴ D. Kaczorowski and T. Komatsubara, *Physica B* **403**, 1362 (2008).
- ¹⁵ A. P. Pikul and D. Kaczorowski, *Acta Phys. Pol. A* **115**, 235 (2009).
- ¹⁶ G. M. Sheldrick (1997), *SHELXL-97*, Program for crystal structure refinement, University of Göttingen, Germany.
- ¹⁷ J. S. Hwang, K. J. Lin, and C. Tien, *Rev. Sci. Instrum.* **68**, 94 (1997).
- ¹⁸ P. Hohenberg and W. Kohn, *Phys. Rev.* **136**, B864 (1964).
- ¹⁹ P. Blaha, K. Schwarz, G. K. H. Madsen, D. Kvasnicka, and J. Luitz, *WIEN2k, An Augmented Plane Wave + Local Orbitals Program for Calculating Crystal Properties* (Karlheinz Schwarz, Techn. Universität Wien, Austria, 2001).
- ²⁰ A. H. MacDonald, W. E. Pickett, and D. D. Koelling, *J. Phys. C* **13**, 2675 (1980).
- ²¹ J. P. Perdew, K. Burke, and M. Ernzerhof, *Phys. Rev. Lett.* **77**, 3865 (1996).
- ²² V. I. Anisimov, I. V. Solovyev, M. A. Korotin, M. T. Czyżyk, and G. A. Sawatzky, *Phys. Rev. B* **48**, 16929 (1993).

- ²³ A. I. Liechtenstein, V. I. Anisimov, and J. Zaanen, *Phys. Rev. B* **52**, R5467 (1995).
- ²⁴ M. S. S. Brooks, *Physica B&C* **130B**, 6 (1985).
- ²⁵ O. Eriksson, B. Johansson, and M. S. S. Brooks, *J. Phys.: Condens. Matter* **1**, 4005 (1989).
- ²⁶ O. Eriksson, M. S. S. Brooks, and B. Johansson, *Phys. Rev. B* **41**, 7311 (1990).
- ²⁷ P. E. Blöchl, O. Jepsen, and O. K. Andersen, *Phys. Rev. B* **49**, 16223 (1994).
- ²⁸ J. J. Yeh and I. Lindau, *Atom. Data Nucl. Data Tables* **32**, 1 (1985).
- ²⁹ K. Cenzual, B. Chabot, and E. Parthe, *Acta Cryst.* **C44**, 221 (1988).
- ³⁰ J. Rossat-Mignod, P. Burlet, J. Villian, H. Bartholin, W. Tchen-Si, D. Florence, and O. Vogt, *Phys. Rev. B* **16**, 440 (1977).
- ³¹ J. Rossat-Mignod, J. M. Effratin, P. Burlet, T. Chattopadhyay, L. P. Renault, H. Bartholin, C. Vettier, O. Vogt, D. RAvot, and J. C. Achart, *J. Magn. Magn. Matter.* **52**, 111 (1985).
- ³² T. Shigeoka, H. Fuji, M. Nishi, Y. Uwatoko, T. Takabatake, I. Oguro, K. Motoya, N. Iwata, and Y. Ito, *J. Phys. Soc. Jpn.* **61**, 4559 (1992).
- ³³ S. L. Budko, Z. Islam, T. A. Wiener, I. R. Fisher, A. H. Lacerda, and P. C. Canfield, *J. Magn. Magn. Mater.* **205**, 53 (1999).
- ³⁴ E. S. R. Gopal, *Specific Heats at Low Temperatures* (Plenum Press, New York, 1966).
- ³⁵ A. Tari, *The Specific Heat of Matter at Low Temperatures* (Imperial College Press, London, 2003).
- ³⁶ M. A. Continentino, S. N. deMedeiros, M. T. D. Orlando, M. B. Fontes, and E. M. Baggio-Saitovitch, *Phys. Rev. B* **64**, 012404 (2001).
- ³⁷ J. Mulak and Z. Gajek, *The Effective Crystal Field Potential* (Elsevier, Amsterdam, 2000).
- ³⁸ Z. Gajek, *Phys. Rev. B* **72**, 045139 (2005).
- ³⁹ B. G. Wybourne, *Spectroscopic Properties of Rare Earths* (Interscience, New York, 1965).
- ⁴⁰ W. Carnall, G. L. Goodman, K. Rajnak, and R. Rana, *J. Chem. Phys.* **90**, 3443 (1989).
- ⁴¹ H. Lueken, *Magnetochemie* (Tuebner, Stuttgart, 1999).
- ⁴² H. Schilder and H. Lueken, *J. Magn. Magn. Mater.* **281**, 17 (2004).
- ⁴³ W. H. Press, B. P. Flannery, S. A. Teukolsky, and W. T. Vetterling, *Numerical Recipes (Fortran Version)* (Cambridge University Press, Cambridge, 1992).
- ⁴⁴ Program CONDON is free software, covered by the GNU General Public Licence, and is available from <http://www.condon.fh-aachen.de>.
- ⁴⁵ H. Schilder, (Aachen University of Applied Sciences, Aachen, Germany), private communication.

- ⁴⁶ K. Shigetoh, A. Ishida, Y. Ayabe, T. Onimaru, K. Umeo, Y. Muro, K. Motoya, M. Sera, and T. Takabatake, *Phys. Rev. B* **76**, 184429 (2007).
- ⁴⁷ H. Schilder, M. Speldrich, H. Lueken, A. Sutoric, and M. Kanatzidis, *J. Alloys and Comp.* **374**, 249 (2004).
- ⁴⁸ T. S. (Author), E. Bourdreaux, and L. M. (Eds.), *Theory and Applications of Molecular Paramagnetism* (Wiley & Sons, New York, 1976).
- ⁴⁹ O. Gunnarsson and K. Schönhammer, *Phys. Rev. B* **28**, 4315 (1983).
- ⁵⁰ J. C. Fuggle, F. U. Hillebrecht, Z. Żołnierek, R. Lässer, C. Freiburg, O. Gunnarsson, and K. Schönhammer, *Phys. Rev. B* **27**, 7330 (1983).
- ⁵¹ P. W. Anderson, *Phys. Rev.* **124**, 41 (1961).
- ⁵² S. Doniach and M. Sunjić, *J. Phys. C* **3**, 286 (1970).
- ⁵³ A. Ślebarski, T. Zawada, J. Spałek, and A. Jezierski, *Phys. Rev. B* **70**, 235112 (2004).
- ⁵⁴ A. J. Signorelli and R. G. Hayes, *Phys. Rev. B* **8**, 81 (1973).
- ⁵⁵ Y. Baer, R. Hauger, C. Zürcher, M. Campagna, and G. K. Wertheim, *Phys. Rev. B* **18**, 4433 (1978).
- ⁵⁶ G. Andre, P. Bonville, F. Bourée, A. Bombik, M. Kolenda, A. Oleś, A. Pacyna, W. Sikora, and A. Szytuła, *J. Alloys Compd.* **224**, 253 (1995).
- ⁵⁷ D. Gignoux and D. Schmitt, *J. Alloys Compd.* **225**, 423 (1995).
- ⁵⁸ P. Bak, *Rep. Prog. Phys.* **45**, 587 (1982).
- ⁵⁹ E. Morosan, S. Budko, P. Canfield, M. Torikachvili, and A. Lacerda, *J. Magn. Magn. Mater.* **277**, 298 (2004).
- ⁶⁰ P. C. Canfield, B. K. Cho, D. C. Johnston, D. K. Finnemore, and M. F. Hundley, *Physica C* **230**, 397 (1994).
- ⁶¹ P. A. Goddard, J. Singleton, A. L. Lima-Sharma, E. Morosan, S. J. Blundell, S. L. Bud'ko, and P. C. Canfield, *Phys. Rev. B* **75**, 094426 (2007).
- ⁶² B. K. Cho, B. N. Harmon, D. C. Johnston, and P. C. Canfield, *Phys. Rev. B* **53**, 2217 (1996).
- ⁶³ K. D. D. Rathnayaka, D. G. Naugle, B. K. Cho, and P. C. Canfield, *Phys. Rev. B* **53**, 5688 (1996).
- ⁶⁴ P. C. Canfield, S. L. Budko, B. K. Cho, A. Lacerda, D. Farrell, E. Johnston-Halperin, V. A. Kalatsky, and V. L. Pokrovsky, *Phys. Rev. B* **55**, 970 (1997).
- ⁶⁵ A. Amici and P. Thalmeier, *Phys. Rev. B* **57**, 10684 (1998).

- ⁶⁶ V. A. Kalatsky and V. L. Pokrovsky, Phys. Rev. B **57**, 5485 (1998).
- ⁶⁷ A. Galatanu, E. Yamamoto, T. Okubo, M. Yamada, A. Thamizhavel, T. Takeuchi, K. Sugiyama, Y. Inada, and Y. . Onuki, J. Phys.: Condens. Matter **15**, S2187 (2003).
- ⁶⁸ F. Givord, J.-X. Boucherle, E. Lelievre-Berna, and P. Lejay, J. Phys.: Condens. Matter **16**, 1211 (2004).